Supporting Information

Exchange Bias in a Layered Metal–Organic Topological Spin Glass

Ryan A. Murphy, Lucy E. Darago, Michael E. Ziebel, Elizabeth A. Peterson, Edmond W. Zaia, Michael W. Mara, Daniel Lussier, Ever O. Velasquez, David K. Shuh, Jeffrey J. Urban, Jeffrey B. Neaton, Jeffrey R. Long*

*Correspondence to:
Email: jrlong@berkeley.edu

This PDF file includes:

Materials and Methods
Supplementary text
Figures S1 to S21
Tables S1 to S3
SI References

Materials and Methods

General Information

All manipulations of the reported materials were performed inside either the Ar atmosphere of an MBRAUN glovebox or a 95/5% N_2/H_2 atmosphere in a custom VAC Atmospheres glovebox. Infrared spectra were collected on a Perkin Elmer Avatar Spectrum 400 FTIR spectrometer under an atmosphere of N_2. Inductively coupled plasma optical emission spectroscopy (ICP-OES) was carried out at the Microanalytical Laboratory of the University of California using a Perkin Elmer Optima 7000 DV ICP-OES. Samples were digested in 70% nitric acid in water. Benzenehexathiol was synthesized according to a previously published procedure.[1] Dichloromethane was dried using a commercial solvent purification system designed by JC Meyer Solvent Systems. Water obtained from a Milli-Q system was sparged with Ar for 2 h before use. All other reagents were obtained from commercial vendors and used without further purification.

Synthesis of $Mn_3(C_6S_6)$

In an atmosphere of 95% N_2 and 5% H_2, degassed dichloromethane (40 mL) and degassed water (40 mL) were added to a 100 mL reaction vessel. Separately, benzenehexathiol (4.5 mg, 0.017 mmol) was suspended in dichloromethane (4 mL) and added to the bottom of the dichloromethane layer over a period of 20 min. A solution of $Mn(CH_3CO_2)_2$ (25 mg, 0.14 mmol) in water (4 mL) was then added to the water layer over 20 min. After 1 h, a translucent gold film had formed. Longer reaction times resulted in thicker films. After decanting the solvent, $Mn_3(C_6S_6)$ was washed with water, dichloromethane, and methanol before drying under reduced pressure at 50 °C for one day.

Powder X-Ray Diffraction

Under an atmosphere of 95% N_2 and 5% H_2, a film of $Mn_3(C_6S_6)$ was liberated from the organic/water interface, gently ground to a powder, and packed into borosilicate glass capillaries. High resolution X-ray powder diffraction data were collected at the Advanced Photon Source (APS) at Argonne National Laboratory at 298 K, using a wavelength of 0.45241(4) Å. A peak search, followed by indexing via the Single Value Decomposition method,[2] was executed in TOPAS-Academic,[3] allowing for approximate unit cell determination. Materials Studio was employed to model candidate structures.

UV-Visible-NIR Spectroscopy

A sample of $Mn_3(C_6S_6)$ was ground with the non-absorbing matrix $Ba(SO_4)$ and held in a Praying Mantis air-free diffuse reflectance cell. A CARY 5000 spectrophotometer interfaced with Varian Win UV software was used to collected diffuse reflectance spectra. The Kubelka–Munk function $F(R) = ((1-R)^2)/2R$ was applied to the raw diffuse reflectance spectrum to convert to pseudo-absorbance equivalent data.

IR Spectroscopy

Fourier transform infrared (FTIR) spectra were collected on a Perkin Elmer Avatar Spectrum 400 FTIR spectrometer. Attenuated total reflectance FTIR spectra were measured with a Pike attenuated total reflectance accessory. To prepare the transmission FTIR sample, $Mn_3(C_6S_6)$ was ground with Nujol and sandwiched between 2 polished NaCl

optical plates. To prevent sample oxidation, a glovebag was sealed onto the sample stage and purged with N_2 for 1 h before introducing the sample.

Conductivity Measurements

To produce thin films of $Mn_3(C_6S_6)$ for conductivity measurements, the same synthetic protocol was carried out as described above, with a reaction time of 30 min, with the addition of a glass support 0.5 cm below the organic/aqueous interface. After film formation, the organic layer was slowly syringed from the reaction vessel, resulting in deposition of the film onto the glass substrate. For variable temperature pressed pellet measurements, a 370 µm-thick pellet of $Mn_3(C_6S_6)$ was pressed in a custom two-electrode screw cell with copper contacts polished to a mirror finish. The screw cell was sealed using Torr Seal® low vapor pressure epoxy to prevent sample oxidation. Variable temperature conductivity measurements were performed in the sample chamber of a Quantum Design MPMS2 SQUID magnetometer. The screw cell was affixed to a modified sample rod containing two 26 AWG silver coated copper cables sealed at the top of the rod with an air tight Swagelok fitting and a Torr Seal® low vapor pressure epoxy and lowered into the sample chamber. *I-V* profiles (±1 V) at different temperatures were collected using a Bio-Logic SP200 potentiostat. The temperature dependence of the conductivity was best fit to the Efros-Shklovskii variable-range hopping equation

$$\sigma = \sigma_0 e^{-\frac{T_0}{T}^{1/2}}$$

where σ is the conductivity, σ_0 is a pre-exponential factor, and T_0 is the characteristic temperature.[4] For room temperature thin film measurements, the sheet resistance of each film was measured using a home-built probe station with Keithley 2400 Sourcemeters in a four-wire van-der-Pauw configuration. Colloidal silver was used to create electrical contact pads on each film. Ohmic contacts were confirmed before all measurements. For the two measured films, three measurements were performed for each continuous domain (determined by visual inspection), and averaged, and at least three domains were measured for each film. Film thickness was measured by scratching the film and measuring the step height with a Veeco Dektak 150 profilometer. Electrical conductivity was extracted from the sheet resistance and thickness measurements. The Seebeck coefficient (thermopower) was measured using a homemade probe setup. Two Peltier devices (Ferrotec) were placed ~4 mm apart and a single current was passed through them in opposite polarities, causing one device to heat and the other to cool approximately the same amount relative to room temperature. The sample was placed across these two devices such that a thermal gradient was established (thermal paste from Wakefield Thermal S3 Solutions was used to ensure thermal contact), and the resulting open circuit voltage was measured using an Agilent 34401 multimeter. The temperature gradient was measured using two T-type thermocouples mounted in micromanipulators. The magnitude of the temperature gradient is directly related to the amount of current driven through the Peltier devices. Typically, five different gradients were established (allowed to equilibrate for 200 s between temperature changes), with ten voltage measurements taken and averaged at each ΔT. All samples exhibited linear variation of open circuit voltage with ΔT; this trend was used to extract Seebeck coefficient values. Data for both electrical conductivity and Seebeck coefficients were acquired using homemade Labview programs. For each measurement, at least three different samples were measured and averaged.

X-ray photoelectron spectroscopy
Data were collected using a Perkin Elmer PHI 5600 monochromatized XPS instrument with a Mg anode. To prevent oxygen contamination and reactivity, sample preparation and mounting were performed in an argon glovebox. The sample was affixed to a silicon wafer using double sided carbon tape. After mounting the wafer on the stage, the sample was sealed in an airtight jar. To load into the XPS, a glovebag containing the jar was sealed onto the loading chamber and subsequently purged with a high flow of argon for one hour, after which the sample was loaded into the chamber under argon. Samples were calibrated using the aromatic carbon peak as a standard. For proper peak fitting, a Shirley background was applied to regions of interest and subtracted after peak fitting. All data processing and peak fitting was performed using CasaXPS.

Magnetic Measurements
In an Ar filled glovebox, 18.5 mg of $Mn_3(C_6S_6)$ was added to a 5 mm inner diameter (7 mm outer diameter) quartz tube containing a raised quartz platform, along with an equal volume of solid eicosane. The tube was fitted with a Teflon sealable adapter, evacuated on a Schlenk line, and the eicosane was melted in a 40 °C water bath until a homogenous mixture of sample and eicosane was observed. This mixture minimizes particle torqueing and ensures good thermal contact between sample and cryostat. The tube was then flame-sealed under static vacuum. A Quantum Design MPMS2 SQUID magnetometer equipped with a reciprocating sample option (RSO) was used to perform direct current and alternating current magnetic susceptibility measurements. Ac susceptibility data were collected using a 4-Oe switching field. Variable-field magnetization measurements were performed using a sweep rate of 3 mT/s. Diamagnetic corrections of $\chi_D = -0.000168$ emu/mol ($Mn_3(C_6S_6)$) and $\chi_D = -0.00024306$ emu/mol (eicosane) were applied to all data.

Scanning Electron Microscopy
Images were collected using a Hitachi S-5000 microscope operating at 30 kV. To prepare the sample displaying the bottom face of the film, a silicon wafer was lowered (raised) onto the upper (lower) surface of a freshly prepared film suspended at the aqueous/organic interface. The sample displaying the top face of the film was prepared similarly to those used in film conductivity measurements. Samples were sputtered with gold prior to data collection to minimize potential sample charging.

Manganese *K*-edge X-ray Absorption Spectroscopy
Data were collected at the Advanced Light Source bending magnet microprobe beamline 10.3.2 (2.1–17 keV) with the storage ring operating under top-off conditions at 500 mA and 1.9 GeV.[6] $Mn_3(C_6S_6)$ and MnS samples were individually mounted onto Kapton tape in an Ar-filled glovebox, sealed in multiple hermetic bags, transferred to the ALS, and measured in fluorescence mode by continuously scanning the Si(111) monochromator (Quick X-ray absorption spectroscopy mode).[6] Fluorescence emission counts were recorded with a seven-element Ge solid-state detector (Canberra) and XIA electronics. All spectra were collected from 100 eV below and up to 300 eV above the edge and calibrated using a manganese foil, with the first derivative set at 5465.1 eV. All data were processed

using LabVIEW custom software available at the beamline and further processed with Athena.[7]

Computational Methods

First-principles ionic and electronic structure calculations were performed using density functional theory with a plane-wave basis and projector augmented wave (PAW) potentials[8] as implemented by the Vienna *ab-initio* simulation package (VASP).[9,10] All calculations are performed in the generalized gradient approximation as implemented by Perdew, Burke and Ernzerhof (PBE) (56), with the addition of a Hubbard U term (GGA+U)[11] to account for on-site localization on the Mn ions, using U = 4.0 eV. A plane-wave energy cut-off of 500 eV was used with a $10 \times 10 \times 1$ Gamma-centered k-point mesh. A 20 Å vacuum insertion was used to prevent interactions between monolayers. Non-collinear spin polarized ionic relaxations, band structure, and density of states calculations were performed for all magnetic conformations considered, with spin-orbit coupling included. All forces were converged to < 0.001 eV/Å in the structural relaxations. For monolayer calculations, a 20 Å vacuum layer was inserted to prevent interactions between adjacent layers. In the calculated bulk crystal structure, individual layers were directly aligned along the *c*-axis and Grimme-D3 corrections were included to account for interlayer dispersion forces.[12] All forces were converged to < 0.001 eV/Å in the structural relaxations. Non-collinear spin polarized ionic relaxations, band structure, and density of states calculations were performed for all magnetic conformations considered for monolayers, and for the most stable conformation for the bulk structure, with spin-orbit coupling included.

Supplementary Text

Magnetic measurements
The exchange bias field, H_E, was determined by taking the average of the field-intercepts, and the coercivity was found by calculating the difference between the absolute values of the field-intercepts and dividing by two. In any field cooled exchange bias hysteresis loop measurement, the field strength used to field cool is set as the maximum applied absolute field in the hysteresis measurement (i.e., after field cooling at 1 T, the hysteresis curve is measured between +/−1 T).

Magnetization relaxation data were best fit using the stretched exponential decay function $M(t) = M_0\exp(-t/\tau)^{1-n}$.[13,14] Alternative decay functions, namely algebraic [$M(t) = M_0\tau^{-a}$], logarithmic [$M(t) = M_0 - S\cdot\ln(t)$], or Debye exponential relaxation [$M(t) = M_0\exp(-t/\tau)$] functions, did not result in acceptable fits for the observed relaxation behavior.[15] The more parameterized stretched exponential functions $M(t) = M_0\exp(-t/\tau)^{1-n} + S\cdot\ln(t) + M_0$ or $M(t) = M_0 t^{-b}\exp(-t/\tau)^{1-n}$ gave fits that indicated that the excess parameters were not necessary: the functions collapsed to the same values found for the simple stretched exponential decay function, absent the excess parameters.[16] These alternative glassy dynamic functions were developed to better describe the anomalous response associated with clustered dynamics in disordered glasses: in a geometrically frustrated glass, it is unsurprising that these parameters are unnecessary.

The following protocol was used to extract χ_3. The sample was cooled from 50 K under zero field, pausing at each temperature point shown in Figure 6d of the main text. At each temperature, a magnetization curve was measured, sweeping the field from 0 to 2 T and back again. The magnetization, M, in a material with broken time reversal symmetry (such as a spin glass) can be expanded in odd powers of the applied magnetic field, $M(H) = \chi_1 H - \chi_3 H^3 + \chi_5 H^5...$ from which the linear and nonlinear susceptibility terms can be extracted (2). Briefly, the linear susceptibility, χ_1, can be extracted by a simple linear fit to the $M(H)$ curves at low fields, where higher order susceptibility terms are minimal. The nonlinear susceptibility, χ_{nl}, can be then extracted and plotted as $\chi_{nl} = \chi_1 - M/H$, after which χ_3 can be extracted by the same linear fitting process after plotting χ_{nl} versus H^2. Curves were fit below 500 Oe (χ_1) and 1100 Oe (χ_3) to ensure that the resultant susceptibility did not contain significant contributions from higher order susceptibility terms.[17] Example data and fits are shown in Supplementary Figure 20.

Discussion of the Possibility of Minor Loops in $Mn_3(C_6S_6)$
The observed magnetic training effect, temperature dependence of the horizontal hysteretic shift, and large increases in coercivity upon field cooling described in this work for $Mn_3(C_6S_6)$ strongly support the presence of exchange bias in this system.[18-20] However, it is relevant here to comment on minor loop phenomena.[21,22] In particular, a minor loop, collected after cooling of a material under field, may be shifted due to the presence of magnetic domains that are too large to be flipped by the external field. Indeed, in certain cases minor loops have been incorrectly conflated with exchange bias.[23,24] However, given that it is possible to *isothermally* induce exchange bias in $Mn_3(C_6S_6)$ (Fig. 5d, main text), it is clear that the behavior observed here is not the result of such a thermally-mediated effect.

The variable field magnetization curves obtained after cooling under applied fields are shifted significantly off of the ZFC data polarized to an equivalent field, a behavior also at odds with a simple minor loop effect. More generally, the lack of magnetic saturation and field dependence of the bias field observed in $Mn_3(C_6S_6)$ are similar to canonical spin glasses as well as other single-phase exchange bias materials.[18-20] Further, we note that the field dependence of H_C and H_E are dissimilar (Supplementary Figure 14), inconsistent with what is expected due to a minor loop phenomenon: if minor loops were responsible for the observed shifted loops, this dependence would be significantly more symmetric.

While we believe the foregoing points are sufficient to obviate concerns regarding conflating a minor loop phenomenon for exchange bias in the $Mn_3(C_6S_6)$, we include a more semantic discussion as well. To do so, we first invoke the phenomenon of an "effectively" saturated system. An effectively saturated system occurs when the maximum applied field is larger than the anisotropy field of the material, and as a consequence, should no longer exhibit a shifted minor loop artifact due to thermally pinned domains.[21-31]The experimentally derived anisotropy field of isoelectronic potassium iron jarosite is far below the maximum applied fields used in this study, which suggests that the shift in the hysteretic origin observed for $Mn_3(C_6S_6)$ cannot be attributed to a minor loop phenomenon. Indeed, if the observed behavior were due to a minor loop phenomenon, this would suggest that a material containing isotropic, high spin manganese(II) is capable of inducing anisotropy fields above 7 T, which is unreasonable given the likely weak spin-orbit coupling and lack of orbital angular momentum in our material.

A further consequence of our discussion of effective major and minor loops is that a system is effectively saturated (and thus in the effective major loop) if the hysteretic traces for increasing and decreasing fields coalesce. As is apparent in the zero-field cooled hysteresis loops presented in Fig. 4 and Supplementary Figure 13, the loops are effectively closed prior to the maximum field applied for field-cooled measurements. In contrast to the zero-field cooled loops, the field cooled loops are significantly wider. In context, this difference suggests that the anisotropy field is asymmetrically strengthened by cooling under a field, an interpretation that is broadly consistent with our discussion of chiral induction in the main text.

One other possible explanation for this isothermal behavior is the dynamics of this system, but it we show that the dynamics of $Mn_3(C_6S_6)$ are also not responsible for the bias. In particular, magnetization decay curves for $Mn_3(C_6S_6)$ after cooling under a larger field 1 T are independent of t_w (Supplementary Fig. 21), as expected in spin glasses. If relaxation was responsible for the hysteretic shift, sweeping to an applied field of the opposite polarity (-1 T) would reset the magnetic state and result in the zero field-cooled (ZFC) loop. The fact that an exchange bias is instead observed strengthens the case for the more subtle explanation of a dynamic chiral induction of spin texture. Our experiments detailing field annealing with variable time are clear evidence here (Supplemental Fig. 18), as the only difference between the measurements is time: the initial magnetization does not increase, while the exchange bias does. Additionally, we note that if simple relaxation were a sufficient explanation for the isothermal bias, we would expect to see drastically different behavior in the magnetic training effect: both the left and right hysteretic intercepts should trend toward the ZFC loop if the shifted hysteresis loop was evidence only of dynamic behavior.
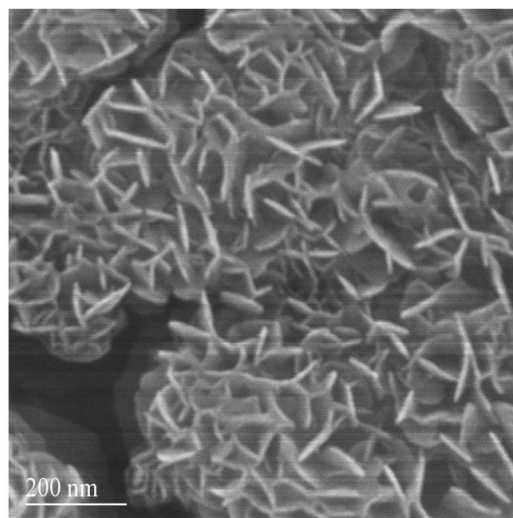
SI Figures:

Supplementary Figure 1: Thin film of $Mn_3(C_6S_6)$ deposited on a glass substrate. Picture on the right is tilted to show thin film interference.
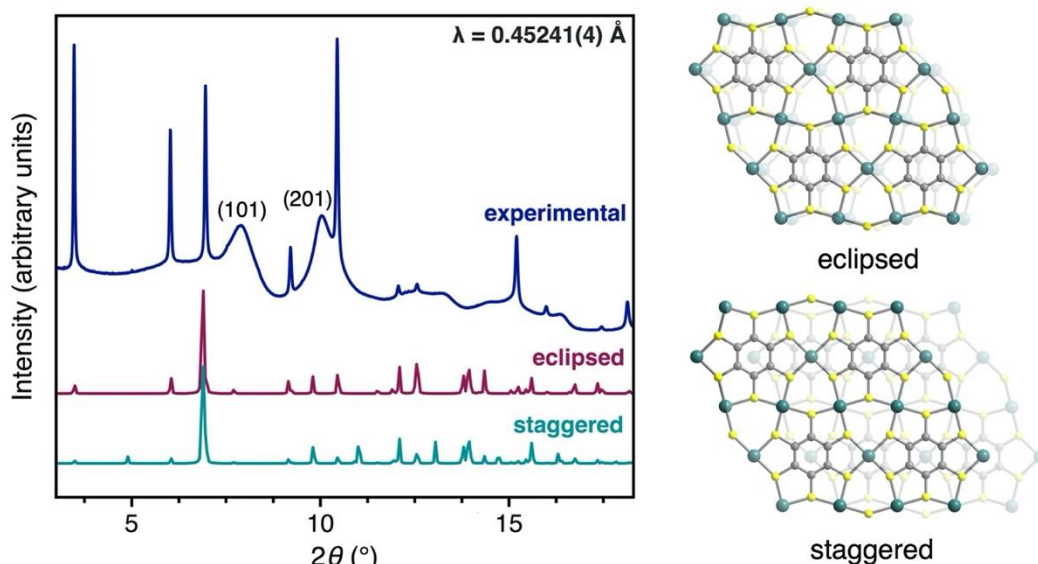
a.

b.

2 µm

200 nm
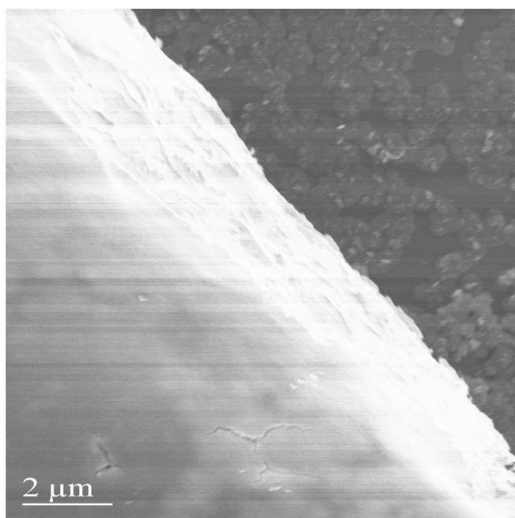
Supplementary Figure 2: Scanning electron microscopy images of $Mn_3(C_6S_6)$. **a.** Smooth surface observed at the organic/aqueous interface. **b.** Rough underside of the thin film, displaying crystallites of $Mn_3(C_6S_6)$.

Supplementary Figure 3: a. Simulated powder X-ray diffraction patterns for models of eclipsed and staggered conformations of $Mn_3(C_6S_6)$ generated in Materials Studio, compared with the experimental data. **b.** Materials Studio models of the eclipsed and staggered conformations.

Our estimation of interplanar spacing is predicated on primary broad peaks at $2\theta \approx$ 8.90 and 10.05°, which have Miller indices of [101] and [201]. Towards disambiguating peak broadening due to particle anisotropy versus disorder, we performed a Scherrer analysis of the (101) peak in the context of our SEM data (SI figure 2). The Scherrer analysis was performed by taking the difference between the peak and the point at which the rate of change of diffraction intensity was ≈ 0 ($2\theta = 8.90°$), and then doubling it to obtain the full width at half maximum (FWHM). The obtained value is 24.26 nm, which corresponds well with the putative z dimension observed in SEM images, suggesting that the experimentally observed particle anisotropy *via* SEM is likely related to the broadening of these peaks. We note that the interplanar distance is ≈ 3.77 Å based on this peak analysis. Considering SI figure 8, where upon pressure-induced pelletization, a major peak consistent with a staggered confirmation is found ($2\theta = 5.18°$ at a wavelength of 0.4969 Å); the interplanar distance associated with that peak is also consistent with this interplanar value. We also note that, as synthesized, the low angle peak associated with the staggered conformation (at $2\theta = 5.01°$) is not well established, indicating to us that there is not sufficient evidence towards a staggered conformation, *absent* pressure, leading to our identification of the as-synthesized phase as eclipsed. This identification is consistent with the observed high intensity, low angle peaks.
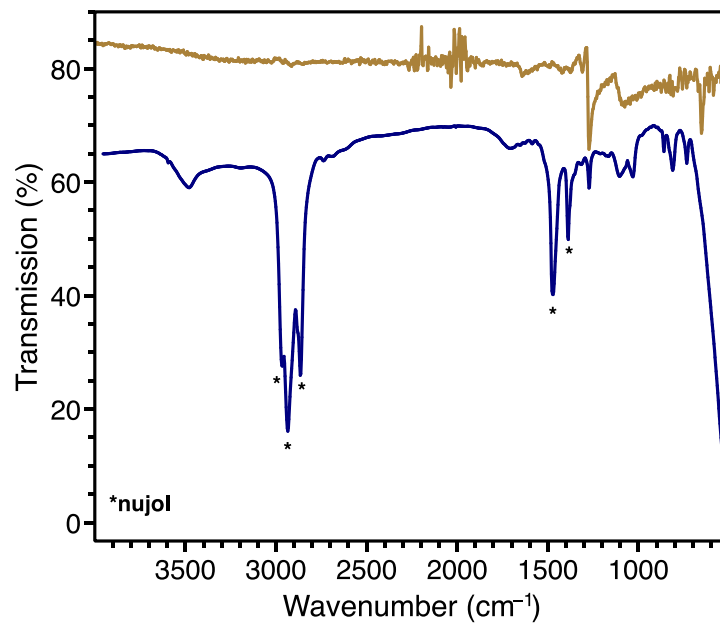
Supplementary Figure 4: Transmission (blue) and attenuated total reflectance Fourier transform infrared (gold) spectra of $Mn_3(C_6S_6)$. Transmission IR data were collected taken in a nujol matrix pressed between polished NaCl optical plates. Starred peaks in the transmission data correspond to peaks from nujol, and the data demonstrate that the nujol peaks do not obscure $Mn_3(C_6S_6)$ peaks.
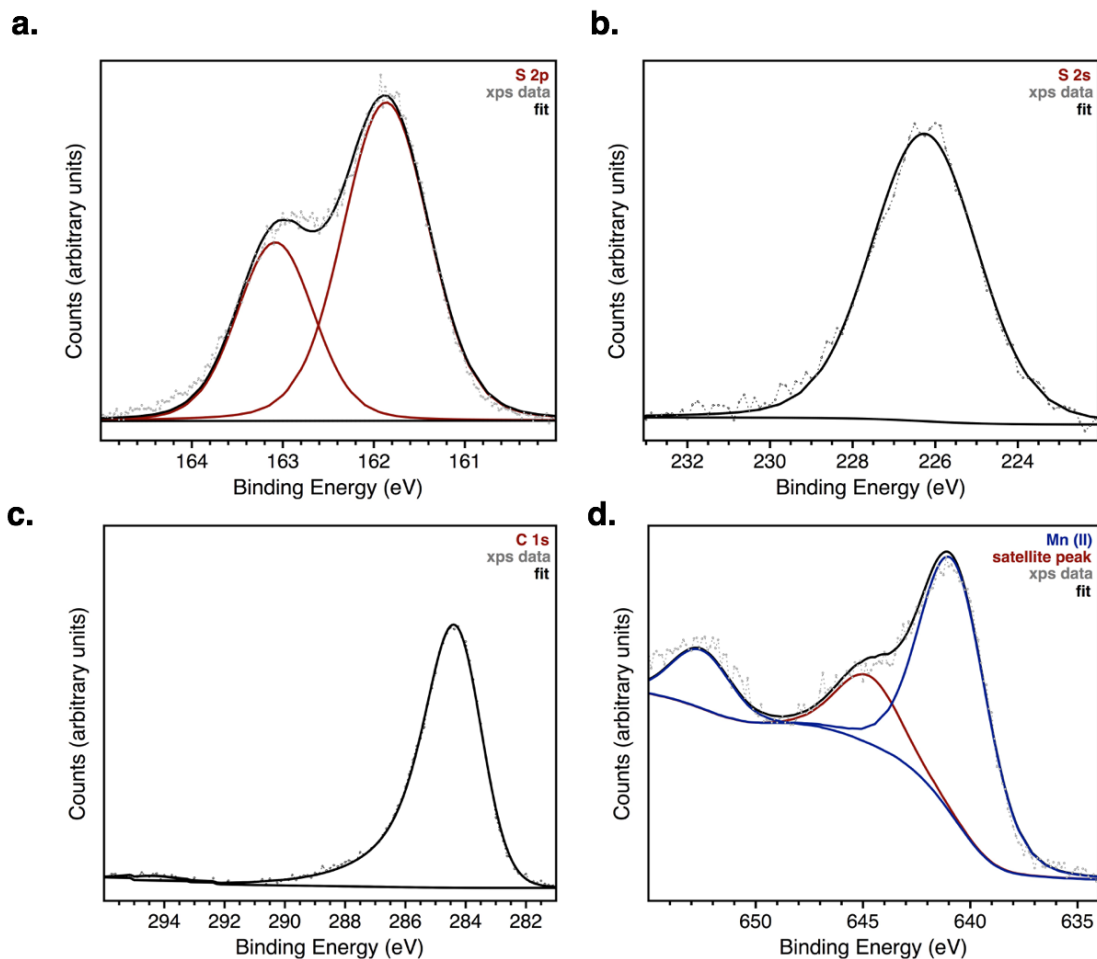
Supplementary Figure 5: Portions of the high-resolution X-ray photoemission spectrum of $Mn_3(C_6S_6)$. Experimental data are given as black dots, and black lines indicate the composite fit. Red lines in 5a represent peaks associated with spin orbit decoupled peaks, while blue lines designate the same in 5d. Red line in 5d represents a satellite peak. **a.** Sulfur 2p, **b.** sulfur 2s, **c.** carbon 1s, and **d.** manganese 2p spectral regions.
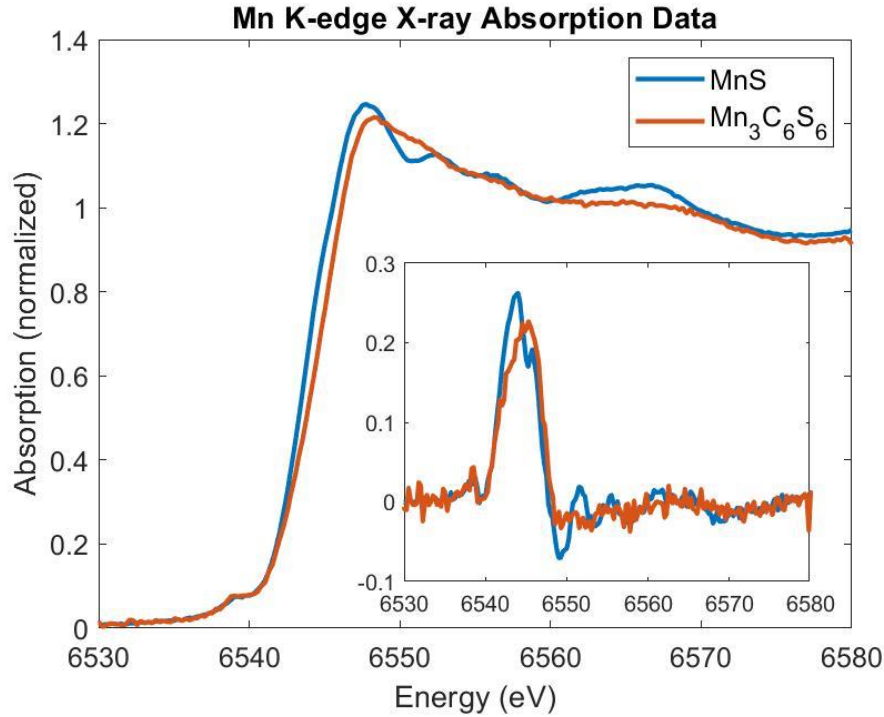
Supplementary Figure 6: X-ray absorption near edge structure (XANES) spectra of $Mn_3(C_6S_6)$ and MnS, with derivatives shown in the inset. The overlap of the derivative spectra indicates that MnS is a good model for the oxidation state of Mn centers in $Mn_3(C_6S_6)$.

Supplementary Table 1: Conductivity (σ) values and Seebeck coefficients determined from measurements on two thin film samples of $Mn_3(C_6S_6)$. For both films, three continuous domains were visually identified, and then measured 3 times to determine the average conductivities reported.

	R_S (kW)	Seebeck coefficient ($\mu V/K$)	Avg. film thickness (nm)	Avg. σ (S/cm)	Power Factor ($\mu W/mK^2$)
Domain 1	127	169	245	0.32	0.92
Domain 2	33.99	166	199	1.48	4.08
Domain 3	1469	165	219	0.03	0.08
Average		167		0.61	1.69

	R_S (kW)	Seebeck coefficient ($\mu V/K$)	Avg. thickness (nm)	Avg. σ (S/cm)	Power Factor ($\mu W/mK^2$)
Domain 1	332.9	109	192	0.16	0.19
Domain 2	270.8	109	125	0.3	0.35
Domain 3	912.6	117	190	0.06	0.08
Average		112		0.173	0.21
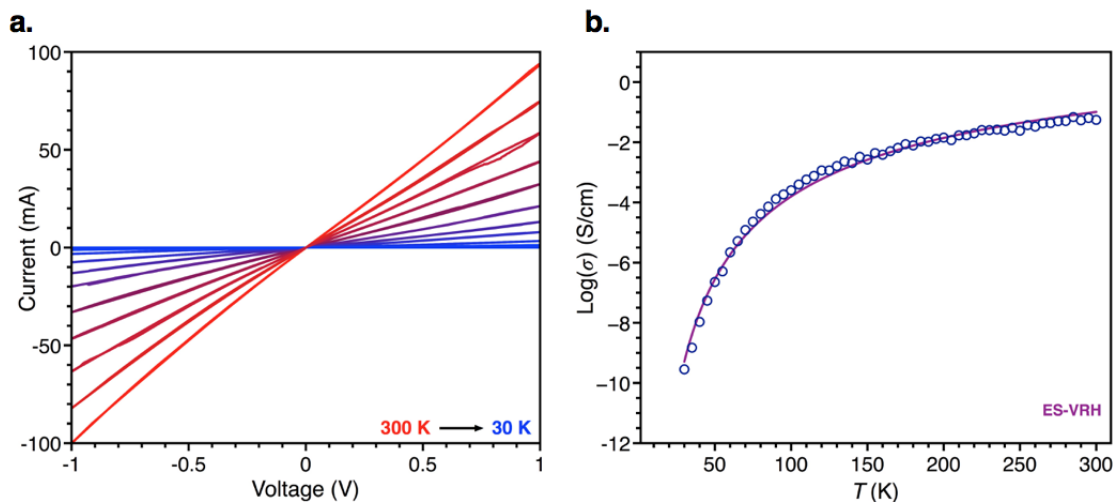
**Supplementary Figure 7: a.** I-V curves of a pressed pellet of $Mn_3(C_6S_6)$ at various temperatures. **b.** Fit to Efros-Shklovskii variable range hopping model.[4]
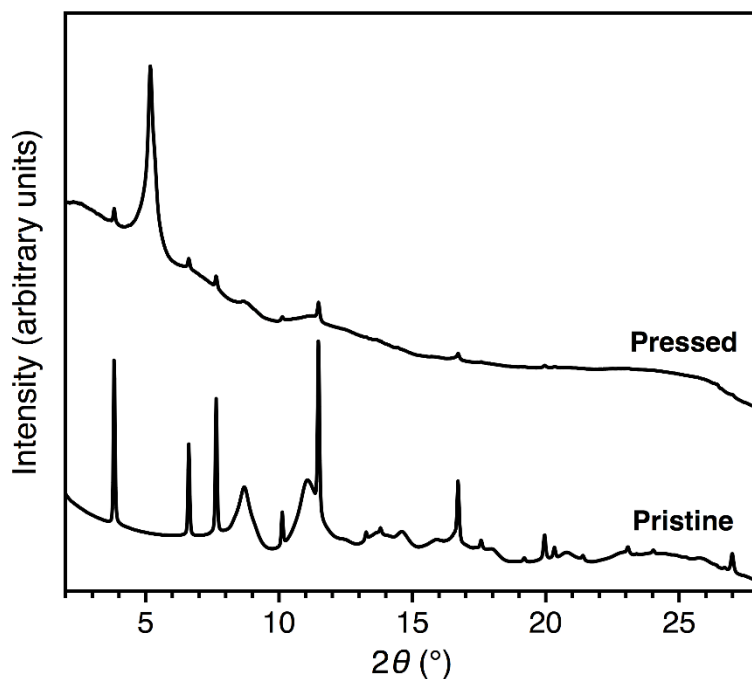

Supplementary Figure 8: Powder X-ray diffraction pattern obtained on a pressed pellet of $Mn_3(C_6S_6)$. Comparison of the data with the diffraction pattern of the as-synthesized material suggests that the pressed pellet undergoes a pressure induced phase change to the staggered stacking conformation. This highlights the necessity of single crystal and/or film measurements. Pattern was taken with wavelength of 0.4969 Å. The peak at $2\theta = 5.18°$ is consistent with the same interplanar distance observed in the as-synthesized material, except here, an eclipsed stacking is a more appropriate fit (see discussion in SI figure 3).
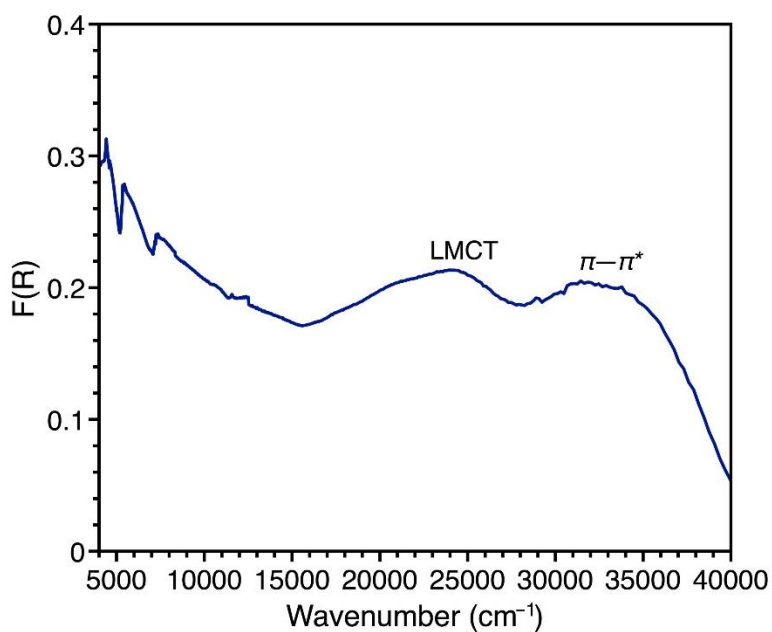
Supplementary Figure 9: Diffuse reflectance UV–Vis–NIR spectrum of $Mn_3(C_6S_6)$. The diffuse reflectance UV–Vis–NIR spectrum of $Mn_3(C_6S_6)$ (Supplementary Fig. 7) displays broad features centered at 24000 and 32500 cm^{-1}, which were assigned to charge-transfer and π-π* ligand-based transitions, respectively, consistent with the benzenehexathiolate species.[32]
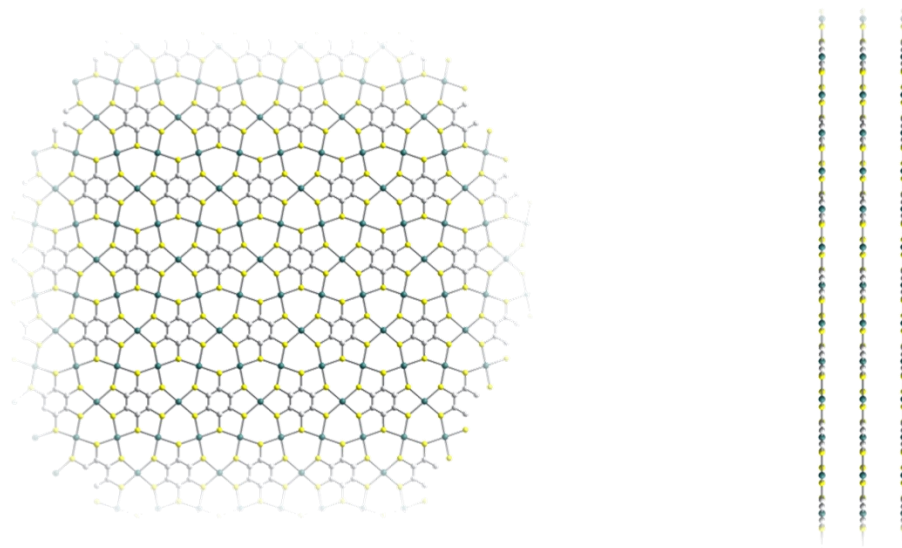
Supplementary Figure 10: DFT optimized eclipsed structure used for bulk band structure and DOS calculations, (*ab* plane on left, stacking conformation on right). Optimized structure has a unit cell of $a = b = 9.1518$ Å, $c = 8.56602$ Å (approximately double the interlayer distance), in reasonable agreement with experimental values.
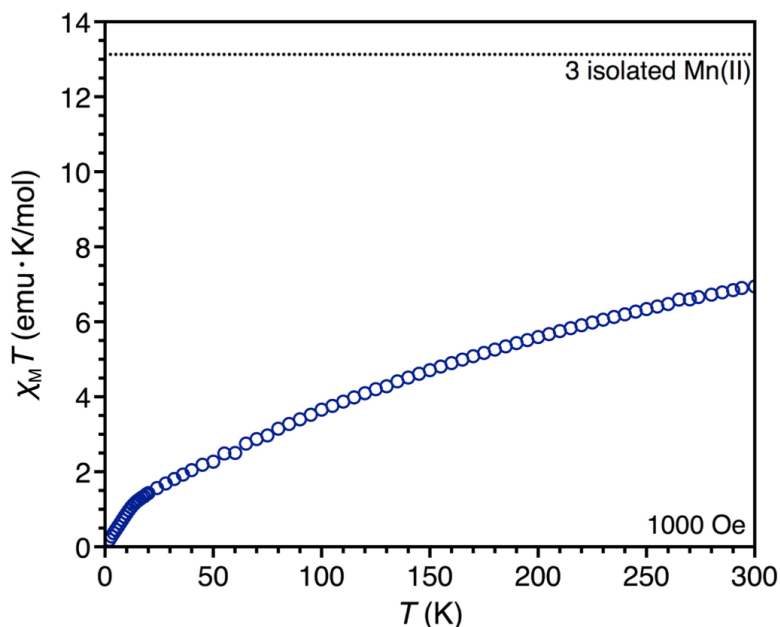
Supplementary Figure 11: Temperature dependence of the molar magnetic susceptibility times temperature, $\chi_M T$, for $Mn_3(C_6S_6)$ under $H_{dc} = 1000$ Oe. Dotted line shows expected value for uncoupled Mn(II) cations (13.13 emu·K /mol). The experimental data indicates a compensated moment of only 6.94 emu·K /mol at room temperature, indicating local antiferromagnetic interactions are persistent even at elevated temperatures.
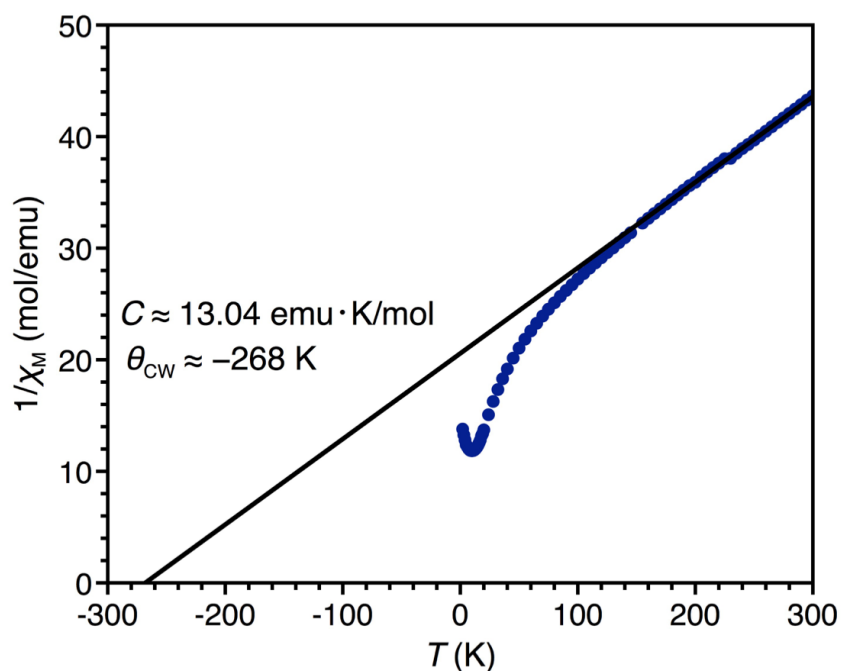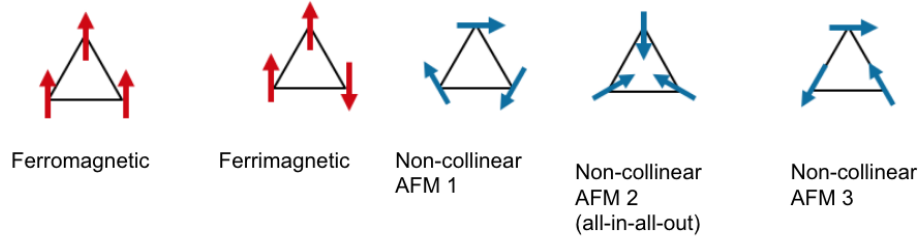

Supplementary Figure 12: Curie-Weiss fit of $Mn_3(C_6S_6)$. Data taken with an applied field of 1000 Oe. Data was fit to $\chi_M = C/(T-\Theta)$, where C is the Curie constant, Θ is the Weiss constant, and T is temperature.

**Supplementary Table 2:** Parameters derived from fitting thermoremanent magnetization decay curves collected after cooling a sample of $Mn_3(C_6S_6)$ from 30 to 2 K under 100 Oe and holding for various wait times, t_w (see Fig. 3d in the main text). The resulting magnetization curves were fit to a stretched exponential as specified above.

t_w (min)	$M_0\,(\mu_B)$	$\tau\,(s)$	n
1	7.73×10^{-4}	1.00×10^{11}	0.829
10	7.74×10^{-4}	5.71×10^{10}	0.822
30	7.735×10^{-4}	2.868×10^{10}	0.812
60	7.743×10^{-4}	2.868×10^{10}	0.812

Supplementary Table 3: (Upper) Comparison of energies of various spin conformations of $Mn_3(C_6S_6)$. (Lower) Monolayer band structure of the lowest energy antiferromagnetic configuration.


Ferromagnetic   Ferrimagnetic   Non-collinear AFM 1   Non-collinear AFM 2 (all-in-all-out)   Non-collinear AFM 3

|	Energy relative to most stable conformation (eV/atom)	Band Gap (eV)
Ferromagnetic	7.839	0.014
Ferrimagnetic	0.956	1.000
Non-collinear AFM 1	0.005	1.539
Non-collinear AFM 2 (all-in-all-out)	0.000	1.539
Non-collinear AFM 3	0.421	1.519
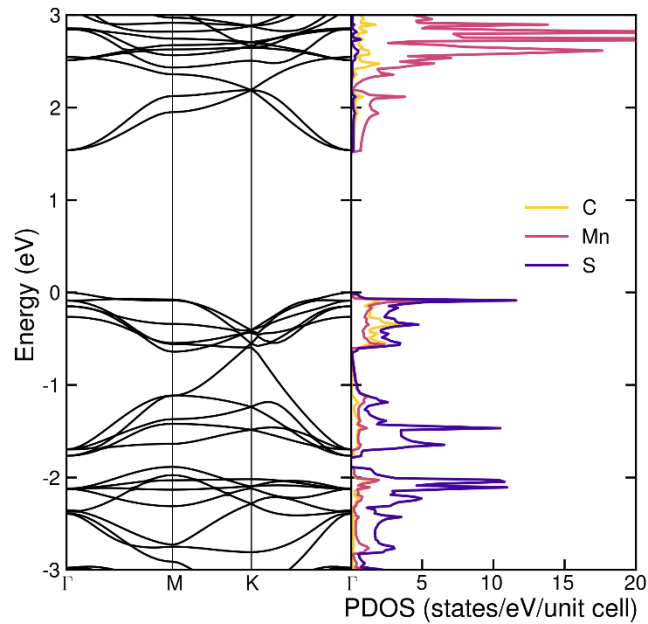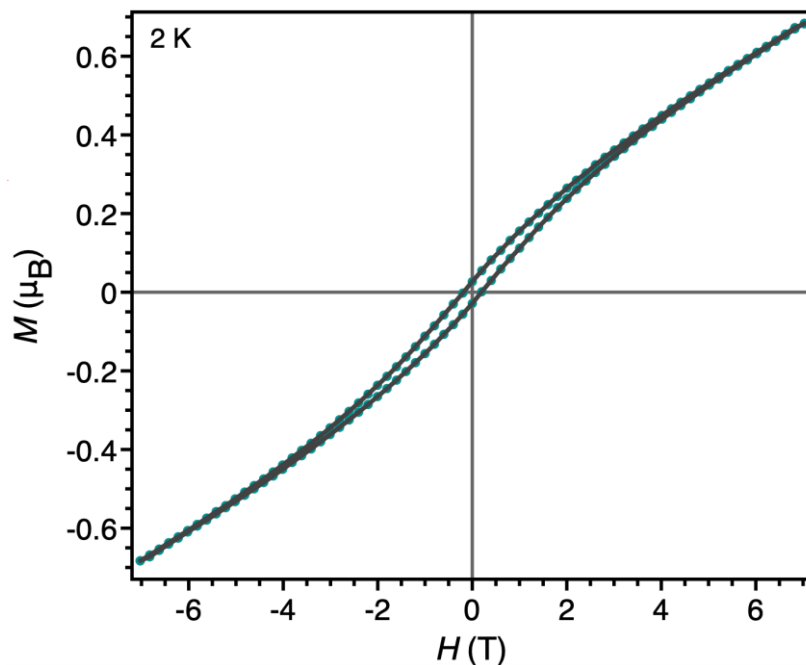
Supplementary Figure 13: Zero-field cooled magnetic hysteresis data collected for $Mn_3(C_6S_6)$ at 2 K.
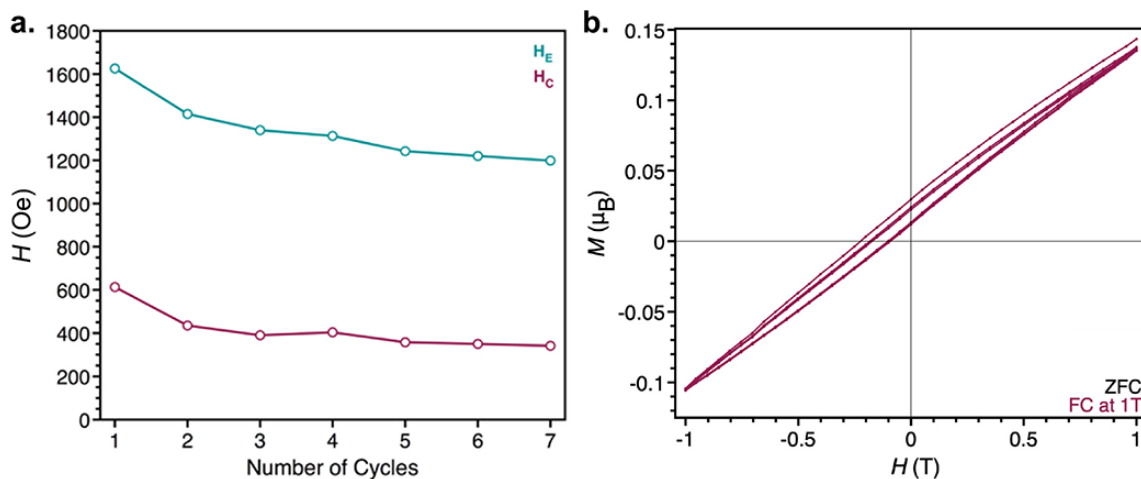

Supplementary Figure 14: a. Change in the values of H_C and H_E with successive hysteresis cycles. Hysteresis data were collected after cooling under 1 T. Data for loops 1-7 were then collected in succession. Solid lines are guides for the eyes. **b.** Representative training loop data. The material was cooled at 1 T, and multiple hysteresis loops were taken afterward.
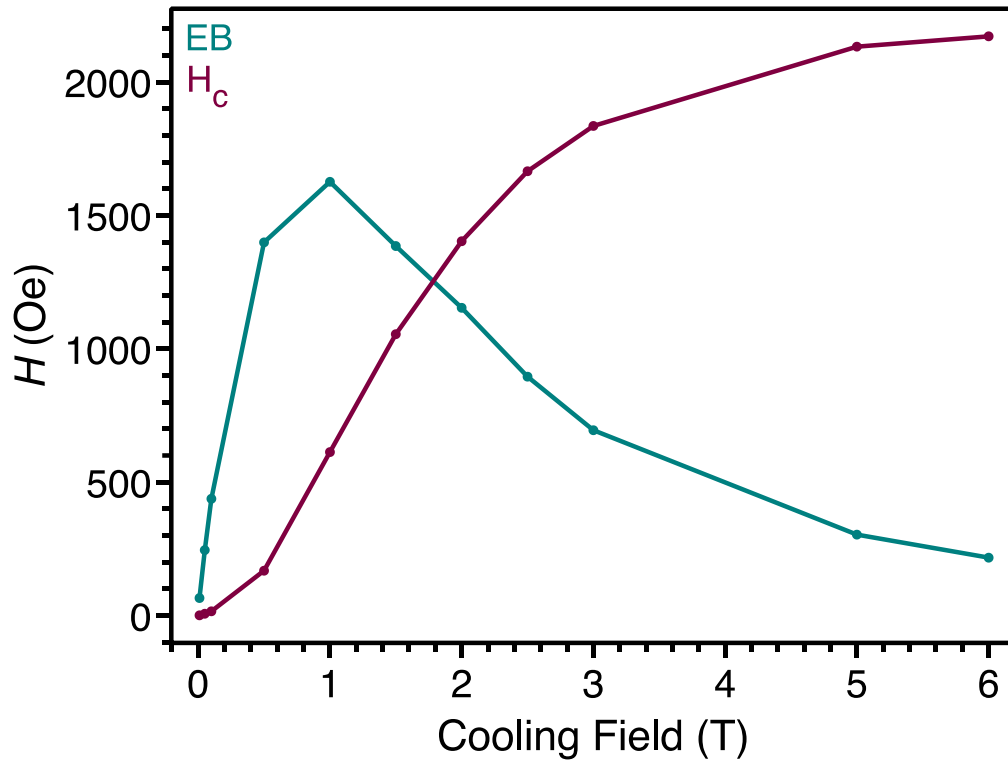
Supplementary Figure 15: Field dependence of exchange bias and coercive fields at 2 K. Solid lines are guides for the eyes.
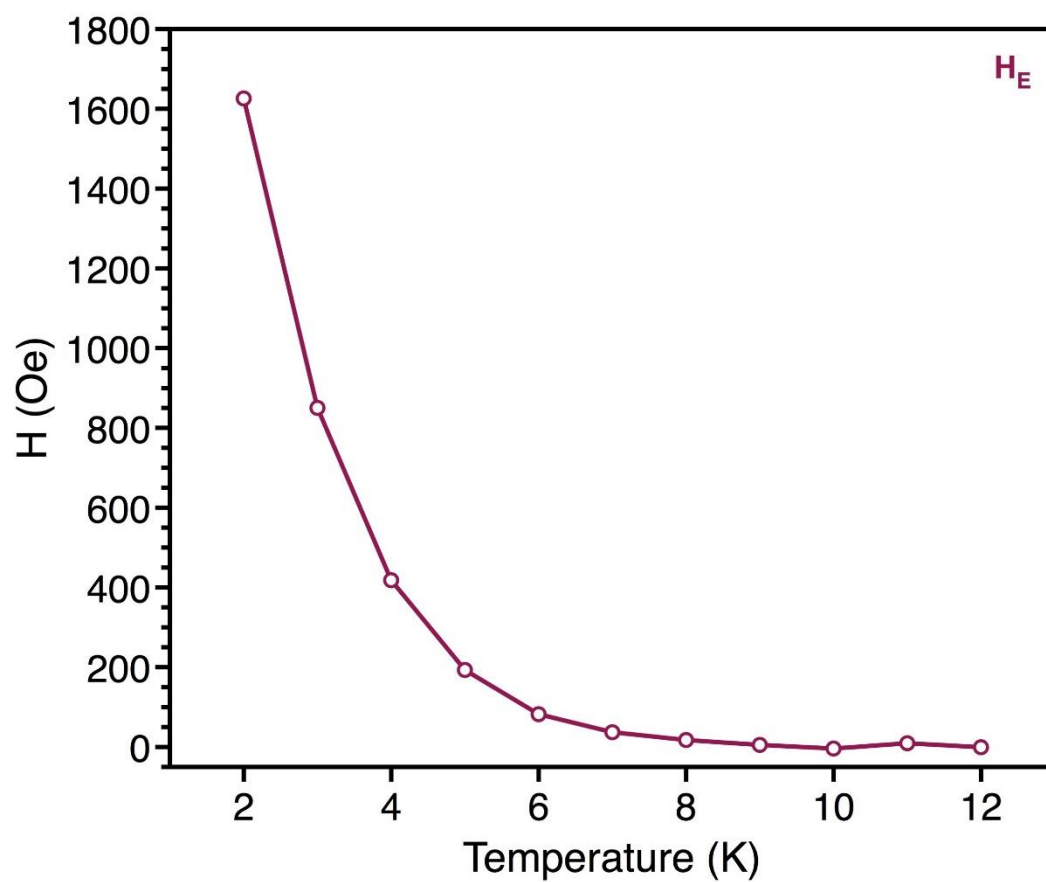
Supplementary Figure 16: Temperature dependence of exchange bias field. The solid line is a guide for the eye. The profile of this trace is consistent with exchange biased systems.[8]
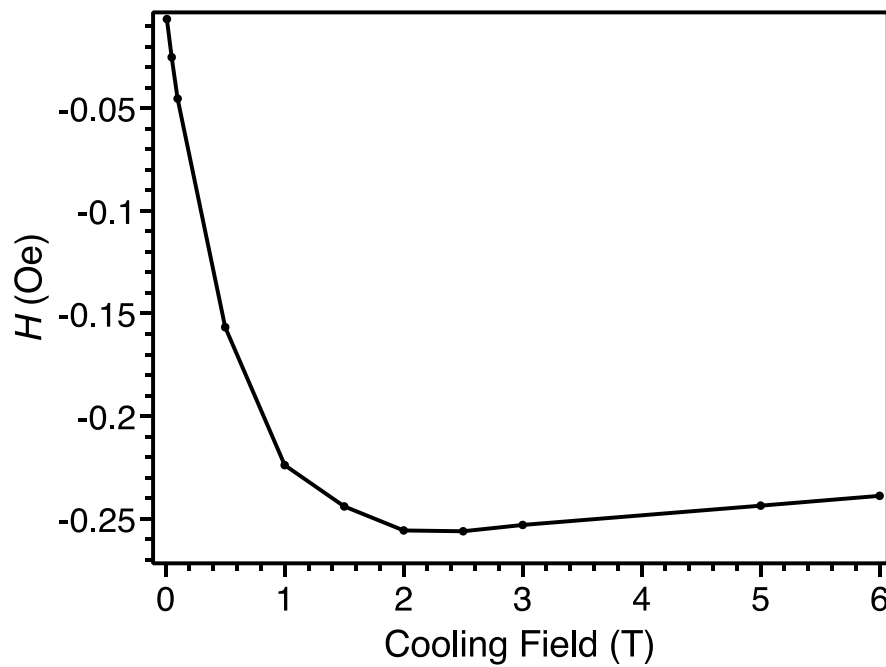
Supplementary Figure 17: Field dependence of the leftmost hysteresis loop intercept as a function of cooling field.
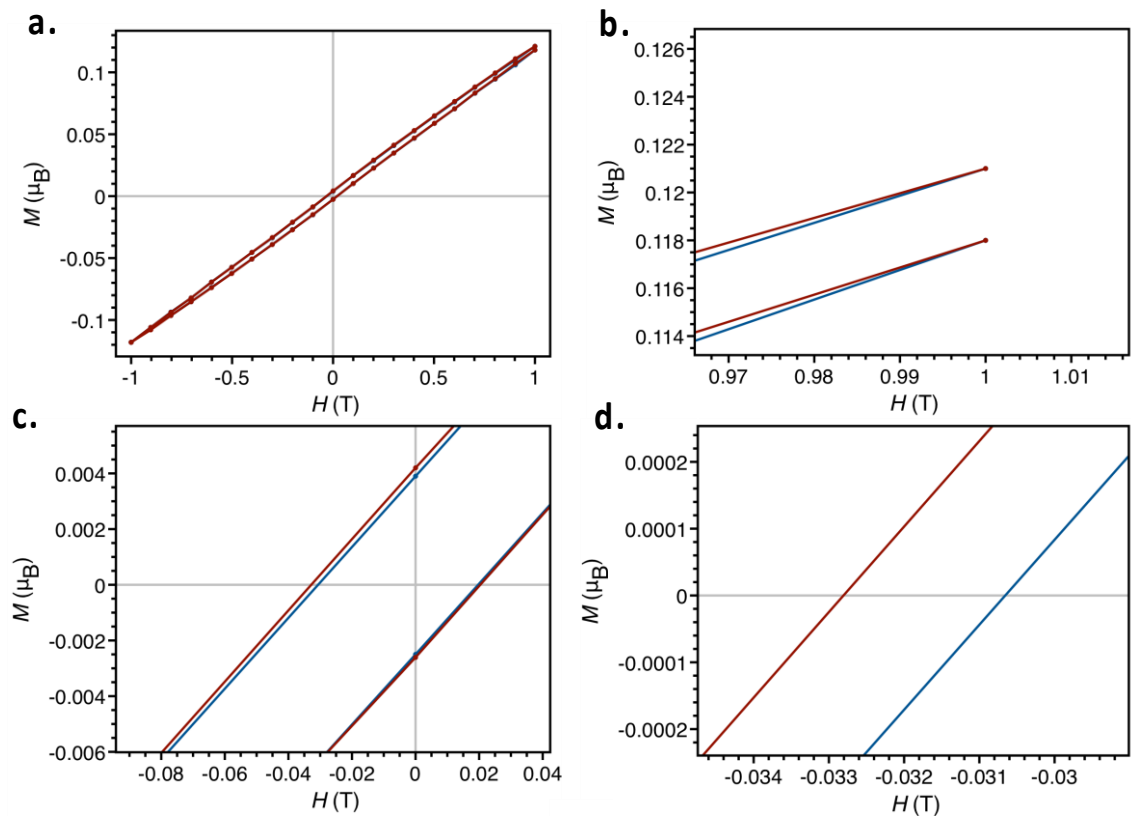
Supplementary Figure 18: Variable-field magnetization data collected after zero-field cooling and subsequently annealing under a 1 T field for 30 sec (blue) and 5 min (red). **a.** Overlap of both loops. **b.** Initial magnetization of the two loops. **c.** Expanded view of the observed exchange bias under both protocols. **d.** Expanded view of leftmost intercept, revealing an increase of 25 Oe between the 30 sec and 5 min data. This increase corresponds to a 14% increase in observed exchange bias.

H₃O·Fe₃(SO₄)₂(OH)₆
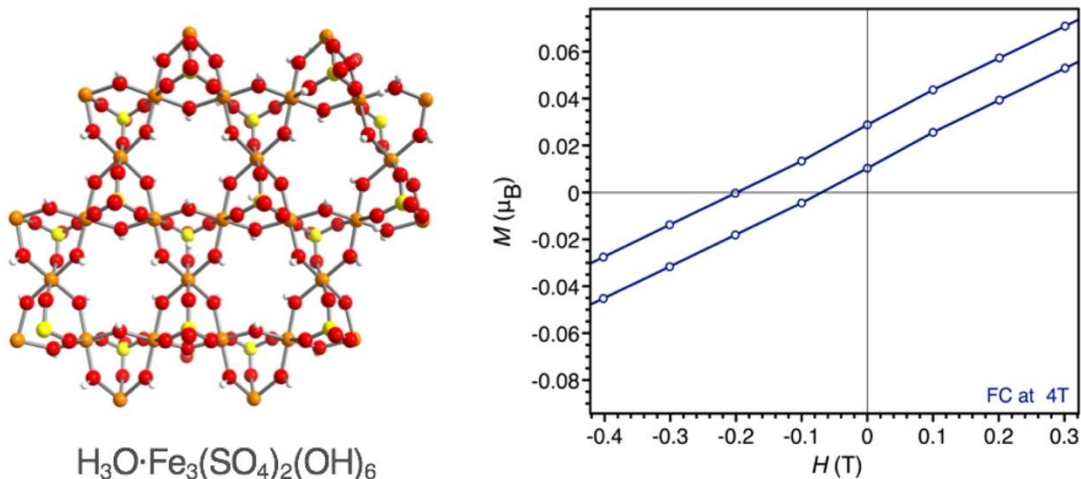
Supplementary Figure 19: Here, we provide an additional demonstration of the viability of geometric frustration toward engendering exchange bias. We synthesized hydronium iron jarosite, a prototypical topological spin glass, via established literature methods.[33] The material was cooled under various fields and variable field magnetization data were collected subsequently, akin to the procedure followed for $Mn_3C_6S_6$. **a.** Kagome structure of hydronium iron jarosite as determined in supplementary reference 21. **b.** The maximum exchange bias (H_E = 1340 Oe) was observed after cooling under a 4 T field.
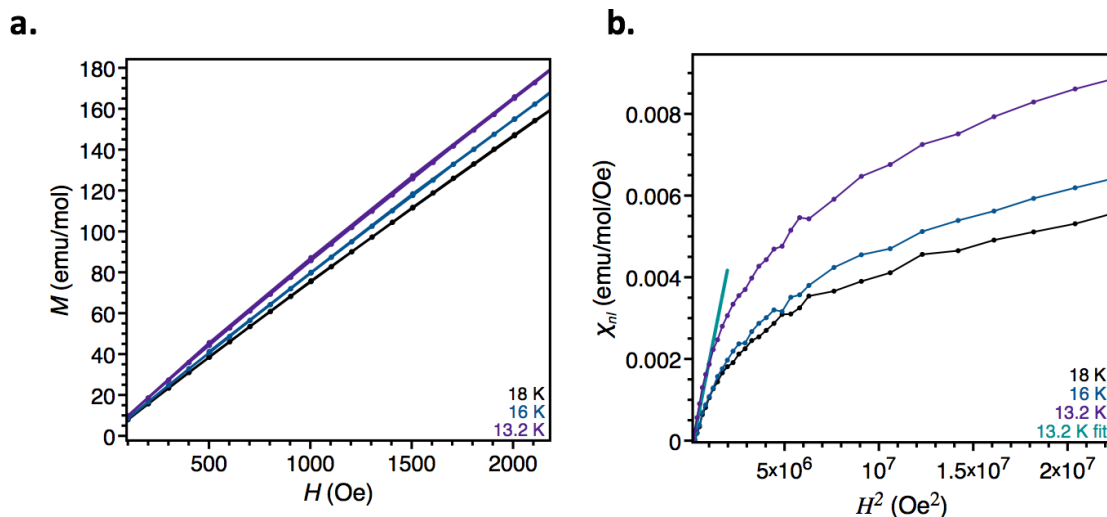
Supplementary Figure 20: a. Example magnetization isotherms used to extract the non-linear susceptibility, χ_{nl}, for $Mn_3C_6S_6$. **b.** χ_{nl} versus H^2 curves used to extract χ_3. An example fit is shown. Fit line was extended for clarity.
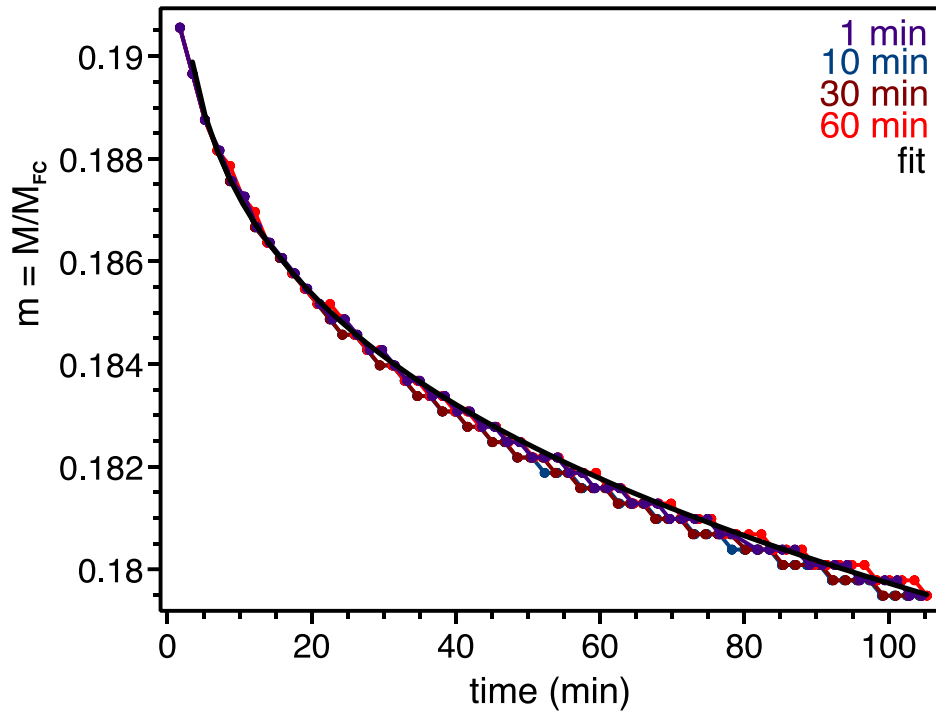
Supplementary Figure 21: Thermoremenant relaxation curves for $Mn_3C_6S_6$ after cooling under a 1 T field with different t_w. The black line is a stretched exponential fit to the data.

References for SI:

1) A. Richter, A. M., Engels, V., Beye, N. & Fanghanel, E. Organische Elektronenleiter und Vorstufen; Zur Darstellung von Hexa-natrium-benzenhexathiolat aus Hexakis-benzylthio-benzen E. *Z. Chem.* **29**, 444-445 (1989).

2) A. Coelho, Indexing of powder diffraction patterns by iterative use of singular value decomposition, *Appl. Cryst.* **36**, 86-95 (2003).

3) A. Coelho, TOPAS-Academic, Version 4.1, Coelho Software, Brisbane, (2007).

4) B. I. Shklovskii, A. L. Efros, *Electronic Properties of Doped Semiconductors* (Springer-Verlag, New York 1984).

5) M. A. Marcus, A. A. MacDowell, R. Celstre, A. Manceau, T. Miller, H .A. Padmore, R. E. Sublett, Beamline 10.3.2 at ALS: a hard X-ray microprobe for environmental and materials sciences, *J. Synchro. Rad.* **11**, 239-247 (2004).

6) S. L. Dudarev, G. A. Botton, S. Y. Savrasov, C. J. Humphreys, A. P. Sutton, Electron-energy-loss spectra and the structural stability of nickel oxide: An LSDA+U study, *Phys. Rev. B* **57**, 1505-1509 (1998).

7) B. Ravel, B. M. Newville, ATHENA, ARTEMIS, HEPHAESTUS: data analysis for X-ray absorption spectroscopy using IFEFFIT. *J. Synchrotron Radiat.* **12**, 537–541 (2005).

8) G. Kresse, D. Joubert, From ultrasoft pseudopotentials to the projector augmented-wave method, *Phys. Rev. B* **59**, 1758-1775 (1999).

9) G. Kresse, J. Furthmüller, Efficiency of ab-initio total energy calculations for metals and semiconductors using a plane-wave basis set, *Comput. Mater. Sci.* **6**, 15-50 (1996).

10) G. Kresse, J. Furthmüller, Efficient iterative schemes for ab initio total-energy calculations using a plane-wave basis set, *Phys. Rev. B* **54**, 169-186 (1996).

11) J. P. Perdew, K. Burke, M. Ernzerhof, Generalized Gradient Approximation made Simple, *Phys. Rev. Lett.*, **77**, 3865–3868 (1996).

12) S. Grimme, J. Antony, S. Ehrlich, H. Krieg, A consistent and accurate *ab initio* parametrization of density functional dispersion correction (DFT-D) for the 94 elements H-Pu *J. Chem. Phys.* **132**, 154104 (2010).

13) R. Chamberlin, G. Mozurkewich, R. Orbach, Time decay of the remanent magnetization in spin-glasses. *Phys. Rev. Lett.* **52**, 867 (1984).

14) G. DeFotis, K. Dell, Thermoremanent-magnetization relaxation in the insulating spin glass $Co_{1-x}Mn_xCl_2 \cdot 2H_2O$. *Phys. Rev. B* **50**, 9937 (1994).

15) J. A. Mydosh, *Spin glasses: An Experimental Introduction* (Taylor and Francis, London 1993).

16) P. Nordblad, P. Svedlindh, L. Lundgren, L. Sandlund, Time decay of the remanent magnetization in a CuMn spin glass. *Phys. Rev. B* **33**, 645 (1986).

17) P. E. Jönsson, R. Mathieu, W. Wernsdorfer, A. M. Tkachuk, B. Barbara, Absence of Conventional Spin-Glass Transition in the Ising Dipolar System $LiHo_xY_{1-x}F_4$. *Phys. Rev. Lett.* **98**, 256403 (2007).

18) A. K. Nayak, *et al*., Design of compensated ferrimagnetic Heusler alloys for giant tunable exchange bias. *Nat. Mater.* **14**, 679-684 (2015).

19) J. Nogues, I. K. Schuller, Exchange bias. *J. Magn. Magn. Mater.* **192**, 203–232 (1999).

20) J. Nogues, *et al*., Exchange bias in nanostructures. *Phys. Rep.* **422**, 65–117 (2005).

21) A. H. Morrish, *The Physical Principles of Magnetism*, (John Wiley & Sons. New York 1965).

22) B. Cullity, *Introduction to Magnetic Materials*, (Addison 1972).

23) L. Klein, Comment on Exchange bias-like phenomenon in SrRuO$_3$ [Appl. Phys. Lett. 88, 102502 (2006)]. *Appl. Phys. Lett*. **89**, 036101 (2006).

24) Pi, L., Zhang, S., Tan, S. & Zhang, Y. Exchange bias-like phenomenon in SrRuO$_3$. *Appl. Phys. Lett.* **88**, 102502 (2006).

25) J. Geshev, Comment on: Exchange bias and vertical shift in CoFe$_2$O$_4$ nanoparticles [J. Magn. Magn. Mater. 313 (2007) 266]. *J. Magn. Magn. Mater.* **320**, 600–602 (2008).

26) J. Geshev, Comment on: Particle size dependent exchange bias and cluster-glass states in LaMn$_{0.7}$Fe$_{0.3}$O$_3$. *J. Phys. Cond. Matt*. **21**, 078001 (2009).

27) W. H. Meiklejohn, C. P. Bean, New magnetic anisotropy. *Phys. Rev*. **102**, 1413 (1956).

28) W. H. Meiklejohn, C. P. Bean, New magnetic anisotropy. *Phys. Rev.* **105**, 904 (1957).

29) W. H. Meiklejohn, W. Exchange anisotropy: a review. *J. Appl. Phys*. **33**, 1328–1335 (1962).

30) Berkowitz, K. Takano, Exchange anisotropy: a review. *J. Magn. Magn. Mater.* **200**, 552–570 (1999).

31) E. Vincent, "Ageing, rejuvenation and memory: the example of spin-glasses." in Ageing and the Glass Transition, M. Henkel, M. Pleimling, R. Sanctuary, Eds. (Springer, 2007) p. 7-60.

32) Y. Shibata, B. Zhu, S. Kume, H. Nishihara, Development of a versatile synthesis method for trinuclear Co(III), Rh(III), and Ir(III) dithiolene complexes, and their crystal structures and multi-step redox properties. *Dalton Trans*. 1939–1935 (2009).

33) S. A. Earle, A. P. Ramirez, R. J. Cava, The Effect of Gallium Substitution for Iron on the Magnetic Properties of Hydronium Iron Jarosite. *Physica B* **262**, 199-204 (1999).